$P_z \approx \pi r_j^2 v_j \sqrt{\rho_a \rho_j}$, where ρ_j, r_j and v_j are respectively the density, radius and velocity of the jet. Therefore we expect the geometry and intensity of the outflow to depend on the location, extent and shape of the region of momentum transfer. Our data show that the largest momentum transfer is occurring closest to the star (less than a few hundred AU) as predicted by jet/shock-driven outflows[21] (and winds[14]). This result is consistent with the region of the highest density being most effective in transferring momentum. However, the density structure at this point is continuously modified owing to evacuation by outflow and accretion from infall. At the initiation of the jet the infall is spherical, the density distribution is broad and the outflow is narrow angled. As the outflow persists, material is swept out of the outflow cones, simultaneously reducing the accretion volume, by narrowing the extent over which infall occurs (Fig. 1). This interaction sets up a negative feedback in that the increase in the opening angle of the outflow cones creates a wider evacuated cavity above the disk–jet interface, and further narrows the equatorial infall. The resulting change in the density structure at the origin of outflow is likely to lead to a momentum transfer occurring in a wider angle. This process continues until the outflow opening angle approaches 180° and the infall is completely shut down.

The idea that the outflow opens up in time, thus blowing away the surrounding envelope and halting infall[22], has remained a conjecture. The data presented here show an interesting possibility of outflow–infall interaction, leading to a change from spherical to an equatorial infall. We have shown that the opening angle of the outflow cones widens with time, which we interpret as a natural mechanism to stop the infall, and hence end the accreting phase in protostars. This observational evidence needs to be considered in theories of formation of stars and disks. □

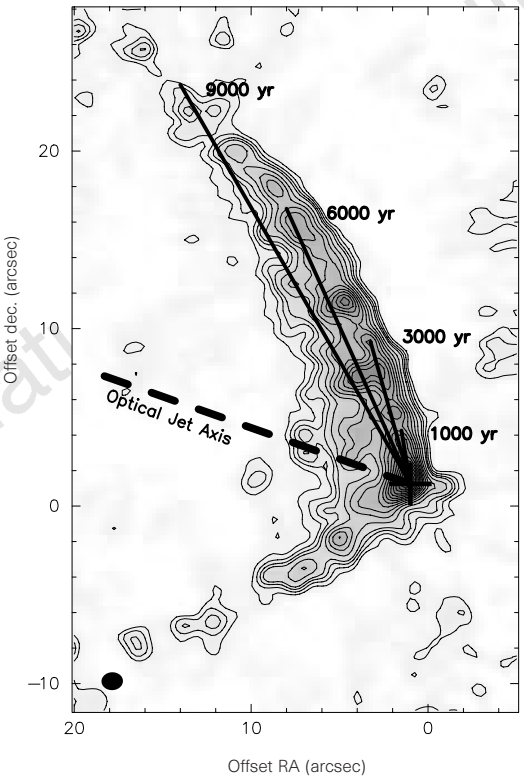

Figure 3 Time evolution of the outflow cones is shown on the integrated intensity map of the blue-shifted outflow lobe. The direction of the jet as inferred from the optical data (which is not seen close to the star but only at parsec scales), is indicated. The first contour is 0.24 Jy km s^{-1} per beam, and contour intervals are 0.24 for the first 6 contours and 0.48 for the rest. The extent of the outflow and direction of gas flow at the epochs shown are derived assuming a mean molecular outflow velocity of 6 km s^{-1}. The widening of the opening angle with time is interpreted as a mechanism to stop infall.

Received 30 September 1997; accepted 14 January 1998.

1. Bontemps, S., Andre, P., Terebey, S. & Cabrit, S. Evolution of outflow activity around low-mass embedded young stellar objects. *Astron. Astrophys.* **311,** 858–872 (1996).
2. Langer, W. D., Velusamy, T. & Xie, T. IRS1 circumstellar disk and the origin of the jet and CO outflow in B5. *Astrophys. J.* **486,** L41–L44 (1996).
3. Chandler, C., Terebey, S., Barsony, M., Moore, T. J. T. & Gautier, T. N. Compact outflows associated with TMC-1 and TMC-1A. *Astrophys. J.* **471,** 308–320 (1996).
4. Chandler, C. & Sargent, A. I. The small scale structure and kinematics of B335. *Astrophys. J.* **486,** L29–L32 (1993).
5. Velusamy, T., Kuiper, T. B. H. & Langer, W. D. Imaging infall: CCS observations of protostellar envelope of B335. *Astrophys. J.* **451,** L75–L78 (1995).
6. Bachiller, R., Guilloteau, S. & Dutry, A. Jet driven molecular outflow in L1448-C. CO and continuum synthesis images. *Astron. Astrophys.* **299,** 857–868 (1995).
7. Gueth, F., Guilloteau, S., Dutrey, A. & Bachiller, R. Structure and kinematics of a protostar: mm-interferometry of L1157. *Astron. Astrophys.* **323,** 943–952 (1997).
8. Ladd, C. J. & Fich, M. The structure and energetics of a highly collimated bipolar outflow: NGC2264G. *Astrophys. J.* **459,** 638–652 (1996).
9. Goldsmith, P. F., Langer, W. D. & Wilson, R. W. Molecular outflows, gas density distribution, and the effects of star formation in the dark cloud Barnard 5. *Astrophys. J.* **303,** L11–L15 (1986).
10. Bally, J., Devine, D. & Alten, V. A parsec-scale Herbig–Haro jet in Barnard 5. *Astrophys. J.* **473,** 921–928 (1996).
11. Stahler, S. The kinematics of molecular outflows. *Astrophys. J.* **422,** 616–620 (1994).
12. Raga, A. c., Cantó, J., Calvert, N., Rodriguez, L. F. & Torrelles, J. M. A unified stellar jet/molecular outflow model. *Astron. Astrophys.* **276,** 539–5482 (1993).
13. Masson, C. R. & Chernin, L. M. Properties of jet-driven molecular outflows. *Astrophys. J.* **414,** 230–241 (1993).
14. Li, Z.-Y. & Shu, F. H. Magnetized singular isothermal toroids. *Astrophys. J.* **472,** 211–224 (1996).
15. Smith, M. D., Suttner, G. & Yorke, H. W. Numerical hydrodynamical simulations of jet-driven bipolar outflows. *Astron. Astrophys.* **323,** 223–230 (1997).
16. Nagar, N. M., Vogel, S. N., Stone, J. M. & Ostriker, E. C. Kinematics of the molecular sheath of the HH111 optical jet. *Astrophys. J.* **482,** L195–L198 (1997).
17. Parker, N. D., Padman, R. & Scott, P. F. Outflows in dark clouds: their role in protostellar evolution. *Mon. Not. R. Astron. Soc.* **252,** 442–461 (1991).
18. Hayashi, M., Ohashi, N. & Miyama, S. A dynamically accreting gas disk around HL Tauri. *Astrophys. J.* **418,** L71–L74 (1993).
19. Burrows, C. J. *et al.* Hubble Space Telescope observations of the disk and jet of HH30. *Astrophys. J.* **473,** 437–451 (1996).
20. Beckwith, S. & Sargent, A. I. Circumstellar disks and the search for neighbouring planetary systems. *Nature* **383,** 139–144 (1996).
21. Chernin, L. M. & Masson, C. R. Momentum distribution in molecular outflows. *Astrophys. J.* **455,** 182–189 (1995).
22. Shu, F., Najita, J., Galli, D., Ostriker, E. & Lizano, S. in *Protostars and Planets III* (eds Levy, E. H. & Lunine, J. I.) 3–45 (Univ. Arizona Press, Tucson, 1993).
23. Beichman, C. A. *et al.* Formation of solar type stars: IRAS observations of the dark cloud Barnard 5. *Astrophys. J.* **278,** L45–L48 (1984).

Acknowledgements. We thank Caltech's OVRO staff for their assistance and support. The Owens Valley Radio Observatory millimeter-wave array is supported by the NSF. This research was conducted at the Jet Propulsion Laboratory, California Institute of Technology, under contract with NASA.

Correspondence should be addressed to T.V. (e-mail: velu@rams.jpl.nasa.gov).

Discovery of a metastable π-state in a superfluid ^{3}He weak link

S. Backhaus, S. Pereverzev, R. W. Simmonds, A. Loshak, J. C. Davis & R. E. Packard

Department of Physics, University of California, Berkeley, California 94720, USA

Under certain circumstances[1,2], a superconducting Josephson junction can maintain a quantum phase difference of π between the two samples that are weakly connected to form the junction. Such systems are called 'π-junctions' and have formed the basis of several experiments designed to investigate the much-debated symmetry of the order parameter of high-temperature superconductors[3–8]. More recently, the possibility that similar phenomena might occur in another macroscopic quantum system—a pair of weakly coupled Bose–Einstein condensates—has also been suggested[9]. Here we report the discovery of a metastable superfluid state, in which a quantum phase difference of π is maintained across a weak link separating two reservoirs of superfluid ^{3}He. The existence of this state, which is the superfluid analogue of a superconducting π-junction, is likely to reflect the underlying '*p*-wave' symmetry of the order parameter of superfluid ^{3}He, but a precise microscopic explanation is at present unknown.

Our experimental apparatus is essentially a container filled with superfluid B-phase ^{3}He and partitioned into two reservoirs by a wall containing both a flexible membrane and a quantum weak link[10], as shown schematically in Fig. 1. The weak link consists of a square array of 4,225 apertures, each of diameter 100 nm, spaced 3 μm apart, and etched through a 50-nm-thick SiN membrane. The membrane, which is coated with a superconducting film, faces a displacement transducer[11] (based on a superconducting quantum interference device, SQUID) that can detect motion of the membrane as small as 10^{-14} mHz$^{-1/2}$. A nearby electrode can be used to move the membrane by the application of voltages between the electrode and the conducting film on its surface. The liquid is in contact with a nuclear demagnetization refrigerator that can cool the ^{3}He to below 200 μK.

The state of each reservoir can be described by a macroscopic quantum wavefunction, which has a well defined quantum phase ϕ (ref. 12). The weak link can be characterized by a function $I(\Delta\phi)$ relating the mass current I to the quantum phase difference $\Delta\phi$ between the two reservoirs. The nature of $I(\Delta\phi)$ at temperature T is determined by the ratio of the individual aperture size to the superfluid healing length $\xi = \xi_0(1 - T/T_c)^{-1/2}$, where $\xi_0 = 65$ nm, and $T_c = 0.929$ mK is the superfluid transition temperature.

Measurements of $I(\Delta\phi)$ are carried out by analysing the time dependence of the position, $x(t)$, of the flexible membrane in response to various applied forces. From this record both $I(t)$ and $\Delta\phi(t)$ can be simultaneously and continuously obtained as follows. The instantaneous mass current through the array is given by:

$$I(t) = \rho A \frac{dx}{dt} \qquad (1)$$

where A is the area of the membrane and ρ is the liquid density. The time dependence of $\Delta\phi$ is given by the Josephson–Anderson phase evolution equation:

$$\Delta\phi(t) = \frac{-2m_3}{\rho\hbar}\int_0^t P(t)dt = \frac{-2m_3k}{\rho\hbar}\int_0^t x(t)dt \qquad (2)$$

where k is the stiffness of the soft membrane (in Pa m^{-1}), $\hbar$ is Planck's constant, m_3 is the atomic mass of ^{3}He, and P is the pressure difference between the two reservoirs. We have previously[10] established an absolute pressure calibration for the constant k by correlating the measured Josephson frequency ($\omega_J = 2m_3P/\rho\hbar$), against the membrane displacement x. It is the result of that measurement that allows the absolute knowledge of the quantum phase difference $\Delta\phi(t)$.

The membrane has a normal mode of oscillation about $\Delta\phi = 0$, whose equations of motion are similar to that of a physical pendulum[13]. In prior measurements of this pendulum mode[14] we found that the full range of $\Delta\phi$, that is, $\pi \rightarrow -\pi$, was inaccessible when the temperature was below approximately 0.48 T/T_c (where ξ is smaller than the aperture diameter). To probe greater values of $\Delta\phi$, we have now developed an experimental method that led to the discovery of the metastable superfluid state reported here. In our present experiment, we excite the oscillator by a few sine-wave cycles of an electrostatically applied, oscillating pressure. The excitation frequency matches the low-amplitude resonant frequency of the pendulum mode. The objective is to pump the pendulum mode to increasingly higher amplitudes to force the system to sample regions of $\Delta\phi$ near $\pm\pi$.

As shown in Fig. 2, a small excitation amplitude drives the oscillator to a small displacement amplitude. After the excitation ends, the oscillation decays slowly (top two traces) due to dissipation associated with the motion of the membrane. As either the number of cycles or the excitation level is increased, the oscillator achieves even larger amplitudes. Finally, an amplitude is reached where the oscillation collapses dramatically to a different mode with a lower amplitude and frequency (lowest trace). After many cycles in this new state, and without any further external drive, the oscillator always makes a second transition back to a state with the same frequency and nearly the same amplitude as the initial state. Thus, during the time interval that the system remains in the low-amplitude mode, the kinetic energy in the original mode must be stored in some other degree of freedom.

The nature of this new state begins to be revealed by using equation (2) to convert $x(t)$ into a plot of $d(\Delta\phi)/dt$ versus $\Delta\phi$. As shown in Fig. 3a, during the excitation section of the experiment, the phase-difference oscillation is centred about $\Delta\phi = 0$. When the oscillation collapses, the measured quantum phase difference is found to make a transition to an oscillation about $\Delta\phi = \pi$. The smaller amplitude of the $\Delta\phi$ oscillation around π is reflected in the smaller radius of the orbits about the new equilibrium. With dissipation, the amplitude of this oscillation can fall to below measurable levels and the system has been observed to remain in this state for more than 15 minutes.

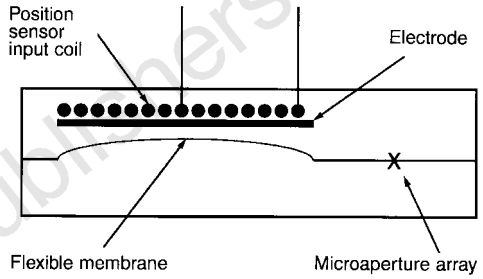

Figure 1 A schematic diagram of the cell. A container filled with superfluid ^{3}He-B is partitioned by a wall containing a flexible membrane and a weak link array.

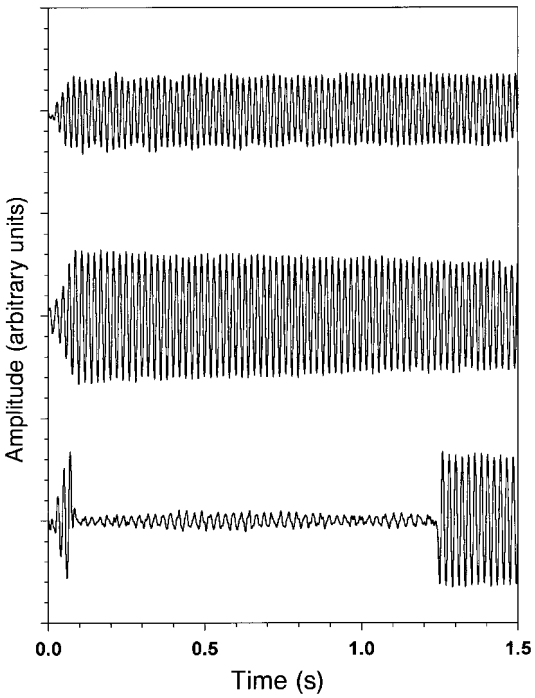

Figure 2 Oscillation of the membrane resulting from the application of 4 cycles of drive at the pendulum-mode resonant frequency, at $0.3T/T_c$. The amplitude of the drive increases from top to bottom. The top two curves show a response similar to that of a high-Q pendulum-like oscillator. The amplitude of motion increases while the drive is applied. After the drive is turned off, the oscillation decays slowly, due to the dissipation associated with the membrane motion. The bottom trace shows the departure from the behaviour of a simple oscillator. The drive level has been adjusted so that the oscillator makes the transition to a new state near the time when the drive is turned off. Without further excitation, the oscillator 'rings' freely in its new state until a random external perturbation causes the transition back to its original state. When the oscillator returns to its original state it regains the energy it had before the collapse.

The location of this new equilibrium has led us to name this state the 'π-state'. By analogy, the equilibrium centred on $\Delta\phi = 0$ is referred to as the 'zero-state'. When the oscillator makes the transition back to its original amplitude and frequency, $\Delta\phi$ is found to switch back to oscillations about either $\Delta\phi = 0$ or 2π. Oscillations about 2π are equivalent to the zero-state owing to the 2π periodicity of $I(\Delta\phi)$. As the two modes of oscillation are about equilibrium points separated by π, we call these sudden changes in the mean phase difference 'π phase slips'.

Using equations (1) and (2), we can compute $I(\Delta\phi)$ over the full range of $\Delta\phi$ directly from data obtained using our experimental technique. The result of such an analysis, shown in Fig. 3b, reveals that a new branch appears in the apparent current–phase relation. The previously unobservable portion of $I(\Delta\phi)$ near $\pm\pi$ is found to lie on the new branch with positive slope centred at $\Delta\phi = \pi$. The horizontal axis in Fig. 3 is the measured phase difference, and includes a contribution from the hydrodynamic inductance near the apertures. It is this component which leads to the multivalued appearance of Fig. 3b and c. If that component is removed, the true $I(\Delta\phi)$ and $F(\Delta\phi)$ are single-valued. However, the dynamics of the system, which are the subject of this work, are determined by the overall phase difference as shown in the figure.

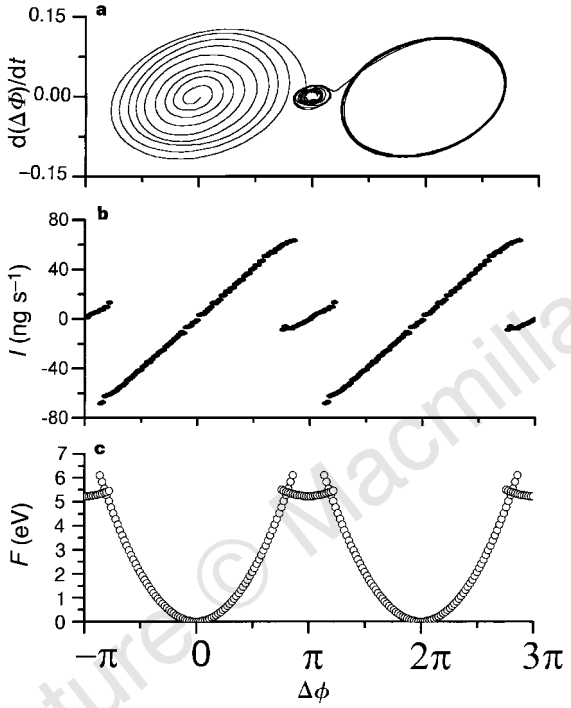

Figure 3 Oscillator characteristics. **a**, Trajectory of the oscillator in the $d\Delta\phi/dt$ versus $\Delta\phi$ plane at $T/T_c = 0.28$. During the drive section of the experiment, the oscillator moves in an increasing radius orbit centred on $\Delta\phi = 0$; this increase is due to the energy input from the drive voltage. At the time the drive is turned off, the system makes a $0 \rightarrow \pi$ transition and orbits about $\Delta\phi = \pi$. The oscillator rings in this state for many cycles (orbits) under the effects of light dissipation. At some time later, an external vibration provides enough energy to put the system into an orbit centred on 2π. This state is equivalent to the state at $\Delta\phi = 0$. **b**, The measured current–phase relation for the microaperture array at $0.28T/T_c$. The vertical axis is the total mass current through the array. The π-branch appears only at temperatures below $0.48\ T/T_c$. At higher temperatures $I(\Delta\phi)$ approaches the sine-function behaviour of a classic Josephson weak link[14]. The maximum value of I at a given value of temperature varies between cool-downs through T_c. This is presumably because of trapped circulation in the array. **c**, The total energy stored in the weak link, F, as a function of $\Delta\phi$ at $0.28T/T_c$. The energy is calculated from the data in Fig. 2b using equation (3). The metastable energy minimum $F(\pi)$ is raised above $F(0)$ by the measured energy jump at the transition $0 \rightarrow \pi$. We note that the horizontal axis represents the phase difference across the complete array and includes a hydrodynamic contribution due to the fluid entering and leaving the array. If this contribution is removed there is no longer an apparent degeneracy in either the energy–phase diagram, or the current–phase diagram.

The implications of this more complete knowledge of $I(\Delta\phi)$ are apparent when one considers the potential energy stored in the weak link. The free energy associated with the weak link is given by[15]:

$$F(\Delta\phi) = \frac{\hbar}{2m_3}\int_0^{\Delta\phi} I(\Delta\phi')\mathrm{d}(\Delta\phi') \qquad (3)$$

The results of calculating F from the experimental data are shown in Fig. 3c. The vertical position of $F(\pi)$ is determined from the apparent energy decrement measured when the zero-state collapses to the π-state.

On referring to Fig. 3c, the interpretation of the motion of the oscillator is clear. Before the excitation is turned on, the system is stationary in its lowest-energy state at $\Delta\phi = 0$. When the oscillatory drive is switched on, it transfers energy to the system causing it to oscillate in the potential-energy minimum centred at $\Delta\phi = 0$. If, at the time when the drive is switched off, the amplitude of oscillation has reached the critical value of $\Delta\phi$ where the two states intersect, the transition $0 \rightarrow \pi$ may occur. With the drive off, and in the presence of only light dissipation, the system oscillates in this new, higher, local minimum centred at π. Although the kinetic energy of the fluid motion in the π-state may eventually dissipate, the energy difference between the two minima is stored in some other degree of freedom of the system and can be released when a transition occurs back to the zero-state. The transition $\pi \rightarrow 0$ occurs when a perturbation, due to vibrations of the cryostat, contributes enough energy so that its oscillation amplitude becomes large enough to allow the transition.

The time the system spends in this new state is not deterministic, although some general observations can be made. At the lowest temperatures, the system can spend many minutes in this state. While at temperatures near $0.48\ T/T_c$ where the state first appears, the time is usually limited to less than 100 ms. The metastability is an unusual feature of our system which will require further research.

A number of situations have been proposed whereby a superconducting Josephson junction can be a 'π-junction'. An early suggestion was for a π-junction in which magnetic scattering of electrons in the junction region flips the spins[1]. The idea of a π-junction was later connected to the symmetry of unconventional superconductors with the suggestion that a closed superconducting loop containing a sample of p-wave superconductor, which is connected to the ordinary superconductor by two Josephson junctions, could contain a π-junction[2]. Elaborations of these ideas have now achieved wide usage in the design of experiments to study the order-parameter symmetry of high-temperature superconductors. These experiments include: (1) SQUIDs formed with junctions on different a–b edges of a crystal of high-temperature superconduction[3,4,15,16], (2) studies of tricrystal rings which have junctions formed by grain boundaries in specific relative orientations[6–8], and (3) junctions between a conventional superconductor in tunnelling contact with both sides of a twin boundary in a high-temperature superconductor[17]. Experiments using these geometries have made significant contributions to knowledge of the symmetry of high-temperature superconductors, and illustrate the importance of the idea of the π-junction.

Recently theoretical studies of Josephson effects between two weakly connected Bose–Einstein condensate (BEC) samples have also revealed the potential for the existence of π-states, which are created when the populations of the two BECs are strongly perturbed by the Josephson current[9].

Superfluid ^{3}He is characterized by a p-wave order parameter[18]. Although there are no crystal axes in this system, the symmetry of

the order parameter may allow locally stable phase differences of π to exist across a weak link between two containers of superfluid ^{3}He. The depth of the observed energy well at $\Delta\phi = \pi$ indicates the existence of a strong term in the $I(\Delta\phi)$ function which is proportional to $\sin(2\Delta\phi)$. The microscopic reason for the existence of this term is so far unknown, and potential explanations in terms of local textures near the apertures, trapped circulation, and internal degrees of freedom of the superfluid will provide fruitful ground for further research.

Note added in proof: It has recently been pointed out[19] that there is a theoretical prediction of a second branch of $I(\Delta\phi)$ at $\Delta\phi = \pi$ in superfluid ^{3}He, when the n-vector fields are antiparallel on opposite sides of the weak link. □

Received 20 November 1997; accepted 16 February 1998.

1. Bulaevskii, L. N., Kuzii, V. V. & Sobyanin, A. A. Superconducting system with weak coupling to the current in the ground state. *JETP Lett.* **25,** 290–293 (1977).
2. Geshkenbein, V. B., Larkin, A. I. & Barone, A. Vortices with half magnetic flux quanta in "heavy fermion" superconductors. *Phys. Rev. B* **36,** 235–238 (1987).
3. Wollman, D. A., Van Harlingen, D. J., Lee, W. C., Ginsberg, D. M. & Legett, A. J. Experimental determination of the superconducting pairing state in YBCO from the phase coherence of YBCO-Pb dc SQUIDs. *Phys. Rev. Lett.* **74,** 797–801 (1993).
4. Brawner, D. A. & Ott, H. R. Evidence for an unconventional superconducting order parameter in $YBa_2Cu_3O_{6.9}$. *Phys. Rev. B* **50,** 6530–6533 (1994).
5. Mathai, A., Gim, Y., Black, R. C., Amar, A. & Wellstood, F. C. Experimental proof of a time-reversal-invariant order parameter with a π phase shift in $YBa_2Cu_3O_{7-\delta}$. *Phys. Rev. Lett.* **74,** 4523–4527 (1995).
6. Tsuei, C. C. *et al*. Pairing symmetry and flux quantization in a tricrystal superconducting ring of $YBa_2Cu_3O_{7-\delta}$. *Phys. Rev. Lett.* **73,** 593–597 (1994).
7. Tsuei, C. C. *et al*. Symmetry of the order parameter of the high-T_c superconductor $YBa_2Cu_3O_{7-\delta}$. *Nature* **373,** 225–229 (1995).
8. Tsuei, C. C. *et al*. Pairing symmetry in single layer tetragonal $Tl_2Ba_2CuO_{6+\delta}$ superconductors. *Science* **271,** 329–332 (1996).
9. Smerzi, A., Fantoni, S., Giovanazzi, S. & Shenoy, S. R. Quantum coherent atomic tunneling between two trapped Bose-Einstein condensates. *Phys. Rev. Lett.* **79,** 4950–4953 (1997).
10. Pereverzev, S. V., Backhaus, S., Loshak, A., Davis, J. C. & Packard, R. E. Quantum oscillations between two weakly coupled reservoirs of superfluid ^{3}He. *Nature* **388,** 449–451 (1997).
11. Paik, H. J. Superconducting tunable-diaphragm transducer for sensitive acceleration measurements. *J. Appl. Phys.* **47,** 1168–1178 (1976).
12. Tilley, D. R. & Tilley, J. *Superfluidity and Superconductivity* (Hilger, New York, 1990).
13. Monien, H. & Tewordt, L. Theory of Josephson flow oscillations in superfluid ^{3}He-B. *J. Low Temp. Phys.* **62,** 277–300 (1986).
14. Backhaus, S., Pereverzev, S. V., Loshak, A., Davis, J. C. & Packard, R. E. Direct measurement of the current–phase relation of a superfluid He-3-B weak link. *Science* **278,** 1435–1438 (1997).
15. Barone, A. & Paterno, G. *Physics and Applications of the Josephson Effect* Section 1.6 (Wiley, New York, 1982).
16. Van Harlingen, D. J. Phase-sensitive tests of the symmetry of the pairing states in the high-temperature superconductors—Evidence for $d_{x^2-y^2}$ symmetry. *Rev. Mod. Phys.* **67,** 515–535 (1997).
17. Kouznetsov, K. A. *et al*. *c*-axis Josephson tunneling between $YBa_2Cu_3O_{7-\delta}$ and Pb: direct evidence for mixed order parameter symmetry in high-Tc superconductors. *Phys. Rev. Lett.* **79,** 3050–3053 (1997).
18. Vollhardt, D. & Wolfle, P. *The Superfluid Phases of Helium-3* Section 7-2 (Taylor & Francis, New York, 1990).
19. Thuneberg, E. V. Two-dimensional Ginzburg–Landau simulation of the Josephson effect in superfluid ^{3}He. *Europhys. Lett.* **7,** 441–446 (1998).

Acknowledgements. We thank D. Rokhsar, D.-H. Lee, S. Vitale, D. Weiss, S. Bahcall, R. Chiao, A. Smerzi and D. J. Van Harlingen for conversations. This work was supported in part by the National Science Foundation, the Office of Naval Research, the Packard Foundation, and the A.P. Sloan Foundation.

Correspondence and requests for materials should be addressed to J.C.D. (e-mail: jcdavis@physics.berkeley.edu).

Phase-mapping of periodically domain-inverted $LiNbO_3$ with coherent X-rays

Z. H. Hu*, P. A. Thomas*, A. Snigirev†, I. Snigireva†, A Souvorov†, P. G. R. Smith‡, G. W. Ross‡ & S. Teat§

* *Department of Physics, University of Warwick, Coventry CV4 7AL, UK*
† *ESRF, BP 220, F-38043 Grenoble, France*
‡ *Optoelectronics Research Centre, University of Southampton, Southampton SO17 1BJ, UK*
§ *Daresbury Laboratory, Warrington WA4 4AD, UK*

A varying refractive index across a wavefront leads to a change in the direction of propagation of the wave[1,2]. This provides the basis for phase-contrast imaging of transparent or weakly absorbing materials with highly coherent X-ray beams[3,4]. Lattice distortions can also change the direction of propagation of a wave field diffracted from a crystal. Here we report the use of this principle to effect phase-contrast imaging of the domain structure of a ferroelectric material, lithium niobate. A periodically domain-inverted structure for quasi-phase-matching of second-harmonic generation is created in this material, in which the direction of spontaneous polarization is sequentially inverted. Because of complex interactions during domain-inversion processing, this is accompanied by lattice distortions across the domain walls. These distortions split the diffracted wavefront of a beam of coherent X-rays from an advanced synchrotron source, giving rise to a pattern of interference that reflects the underlying pattern of lattice distortions. These results show that this phase-contrast imaging technique with sub-micrometre spatial resolution permits the non-destructive, highly sensitive phase-mapping of various structural defects and distortions introduced into materials during processing.

Interference and phase-contrast imaging at optical wavelengths can be conveniently realized by using optical lenses[1]. But this is not the case for hard X-ray wavelengths because the refractive index for X-rays differs from unity by only 10^{-5} to 10^{-6}. Therefore, methods which are free of lenses have been used for X-ray phase-contrast imaging such as the Bonse–Hart interferometer[5] that splits and subsequently recombines coherently-related X-ray beams to generate interference patterns. However, the stringent experimental conditions required with a conventional X-ray source have limited the applications of the phase-contrast imaging technique in research in condensed-matter physics, materials and biological sciences. This technique has recently aroused much interest because the high degree of coherence of intense X-ray beams provided by the European Synchrotron Radiation Facility (Grenoble) has made phase-contrast imaging possible in a convenient manner[4,6,7].

We have explored the possibility of phase-contrast imaging of periodic domain inversion in ferroelectric nonlinear optical materials. Periodic domain inversion refers to the deliberate introduction of a periodic array of domains of alternating structural polarity into a polar crystal, displacing the cations and anions of the structure by applying an external electric field such that the resulting spontaneous polarization is reversed with respect to the original. This generates a spatially periodic modulation of the nonlinear coefficient along the direction of wave propagation that enables quasi-phase-matching of any frequency-doubling interaction within the transparency range of the crystal according to the choice of the period of modulation[8]. Lattice distortions occur during domain-inversion processing because of complex interactions between the physical effects taking place, for example, the converse piezoelectric and/or pyroelectric effects, and the dynamic process of domain inversion[9–11].

The crystal used for our studies is $LiNbO_3$. A domain-inverted structure of period 30 μm was fabricated in a $LiNbO_3$ sample with a thickness of 200 μm via electric-field poling. A synchrotron-radiation X-ray experiment was performed at the ESRF optics beamline (BL10/D5) which is on a bending magnet. The experimental configuration is schematically shown in Fig. 1.

Sets of synchrotron X-ray images of the 0 0 6 symmetric reflection are shown in Fig. 2a–e. Periodic-contrast lines appear with alternating spacings of 22 and 8 μm in Fig. 2a which was taken with a film positioned ~5 mm away from the sample. They are images of the periodic inversion-domain walls. The vertical black-white lines or dots are images of segments or outcrops of dislocations. As the film-to-sample distance increases, the intensity variations become stronger, as shown in Fig. 2b–e. Furthermore, extra fringes appear in the domain-inverted regions of Fig. 2b–e compared with those of Fig. 2a. Clearly, the intensity variations observed above cannot be explained simply by a diffraction imaging or topographic effect. Instead, they mainly arise from interference, that is, the fringe patterns observed in Fig. 2b–e arise from phase contrast. As shown in Fig. 2a and e, the interference fringes run parallel to the domain